Microstructural characterization of high-thermal-conductivity SiC ceramics

Hiromi Nakano [a,*], Koji Watari [b], Yoshiaki Kinemuchi [b], Kozo Ishizaki [c], Kazuyori Urabe [d]

[a] *Electron Microscope Laboratory, Ryukoku University, Seta, Otsu 520-2194, Japan*
[b] *National Institute of Advanced Industrial Science and Technology (AIST), Shimo-shidami, Moriyama-ku, Nagoya 463-8560, Japan*
[c] *School of Mechanical Engineering, Nagaoka University of Technology, Nagaoka 940-2188, Japan*
[d] *Department of Materials Chemistry, Ryukoku University, Seta, Otsu 520-2194, Japan*

Abstract

High-thermal-conductivity SiC ceramic with very small amount of BeO additive, having a value of $270\,W\,m^{-1}\,K^{-1}$ corresponding to roughly 50% of the intrinsic SiC value of $490\,W\,m^{-1}\,K^{-1}$, is characterized by high-resolution transmission electron microscopy. Crack in BeO crystalline phase, strain contrast between BeO and SiC, and stacking disorders in SiC grains are observed, and they are considered as reducing factors on the thermal conductivity. Presence of secondary phase including Fe, Ti, Al and Ni elements and Be_2SiO_4 phase reveals that liquid in the $BeO–SiO_2–SiC$ system forms partially, traps metal impurities to purify SiC grains and precipitates at triple-grain junctions. A distinctive feature of intergranular film between the SiC grains is also reported.
© 2004 Elsevier Ltd. All rights reserved.

Keywords: Sintering; Electron microscopy; Grain boundaries; Thermal conductivity; SiC

1. Introduction

SiC ceramics possess excellent mechanical strength, high oxidation resistance at high temperature, high corrosion resistance, high-thermal shock, and high-thermal conductivity. Accordingly, there is much interest in these materials within the engineering component industry. In recent years, the combination of high-thermal conductivity, high-thermal shock, and high corrosion resistance has accelerated the application of SiC ceramics in semiconductor processing equipment components.[1] Furthermore, SiC ceramics with high-thermal conductivities ($>200\,W\,m^{-1}\,K^{-1}$) have been employed as electronic substrates for highly integrated circuits and laser-reading devices.[2]

The maximum experimental value in SiC ceramics at room temperature is reported to be approximately $270\,W\,m^{-1}\,K^{-1}$,[3,4] representing roughly 50% of the intrinsic crystal value ($490\,W\,m^{-1}\,K^{-1}$.[5] The ceramic was obtained by hot-pressing with a Be dopant.[3,4] In previous work,[6] we measured the thermal conductivity of the ce-

ramic at temperatures between 5 and 1300 K. Moreover, the thermal conductivity mechanism of SiC ceramics has been discussed through calculation of the phonon mean free path and the significance of its temperature variation for the thermal conductivity. We concluded that at temperatures less than 30 K, the conductivities are controlled by the grain boundaries and grain junctions. At temperatures between 30 and 800 K, type and quantity of impurity atoms dissolved in the lattice influence significantly the conductivities.[6] However, direct evidence with respect to the mechanism has not obtained in our work.

In this present work, the microstructure of high-thermal conductivity SiC ceramic is determined in detail by using a transmission electron microscope (TEM). The relationship between the thermal conductivity and the microstructure will be discussed.

2. Experimental

A commercial α-SiC powder with 2 μm sizes (Fujimi Adrasive Co., Ltd., Japan) was mixed with BeO powder as a sintering aid. The mixed powder was pressed with

* Corresponding author. Tel.: +81-77-543-7774.
E-mail address: hiromi@rins.ryukoku.ac.jp (H. Nakano).

a carbon-steel die (50 mm diameter) and followed by hot pressing at 2313 K for 1 h under 20 MPa.[3,4] The thermal conductivity values between 5 and 300 K and between 300 and 1300 K were measured using a steady-state longitudinal heat flow technique and laser-flash technique, respectively.[6]

Phase composition of the sample was identified by X-ray diffractometry (XRD). The oxygen and nitrogen contents of the ceramic were measured using a hot-gas extraction oxygen/nitrogen analyzer (TC-136, Leco Co., USA). Other elements in the ceramic were measured using ICP-AES. A TEM foil was prepared by the standard technique used for preparing the thin foils of ceramics: cutting, grinding, dimpling, Ar-ion thinning, and carbon coating to minimize the electric charging under the irradiated electron beam. Microstructural characterization of the product was performed with a TEM (JEOL-3000F) device, which makes it possible to provide electron probes with a full width at half maximum (FWHM) of around 0.5 nm and also with sufficiently high current for a point analysis by energy dispersive X-ray spectroscopy (EDS).

3. Results

Fig. 1 shows the thermal conductivity of obtained SiC ceramic at 5–1300 K. For comparison, data for single crystal SiC (R66)[5] is also plotted in the same figure. The conductivity of the ceramic is $1.6 \, \mathrm{W \, m^{-1} \, K^{-1}}$ at 5 K, $14 \, \mathrm{W \, m^{-1} \, K^{-1}}$ at 10 K, $140 \, \mathrm{W \, m^{-1} \, K^{-1}}$ at 30 K, $393 \, \mathrm{W \, m^{-1} \, K^{-1}}$ at 60 K, $631 \, \mathrm{W \, m^{-1} \, K^{-1}}$ at 100 K, $402 \, \mathrm{W \, m^{-1} \, K^{-1}}$ at 240 K, $270 \, \mathrm{W \, m^{-1} \, K^{-1}}$ at 300 K, $85 \, \mathrm{W \, m^{-1} \, K^{-1}}$ at 800 K, and $50 \, \mathrm{W \, m^{-1} \, K^{-1}}$ at 1300 K.[6] Below 800 K, the difference in the value of the thermal conductivity appeared between a single crystal and a SiC ceramic doped with BeO, as seen in Fig. 1. The difference should be caused from the structure
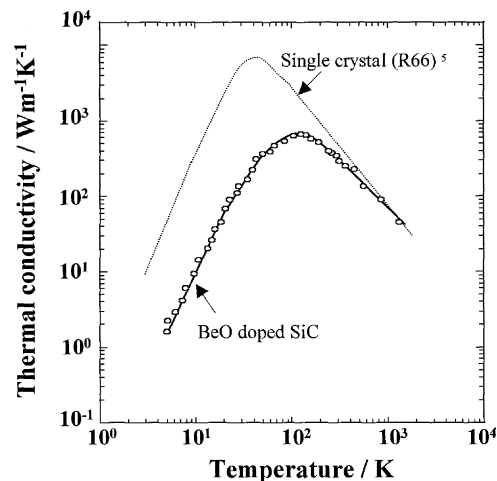

Fig. 1. Temperature dependence of thermal conductivity of single crystal SiC (R66) and polycrystalline SiC doped with BeO.

of polycrystalline SiC ceramic. Then, we observed carefully the microstructure of the obtained SiC ceramic.

Fig. 2 shows low-magnification TEM images of the polycrystalline SiC. Most grains were densely packed and the grain boundaries were oriented randomly, as seen in Fig. 2(a). Additionally, a contrast between stripes due to stacking disorders was clearly observed in the grains. The main Peaks in the XRD pattern of the SiC were determined as corresponding to the structures of 6H- and 4H-SiC. However, the contrast in the TEM image indicated the existence of other types of polytype in the grain. Some secondary phases were observed at triple-grain junctions and even in the grain, as indicated by arrows in Fig. 2(b). Most of the secondary phase was a BeO crystalline phase, whose small peak was detected by XRD measurement. The secondary phase in the grain might remain during the growth of the two grains. Table 1 shows the chemical compositions of
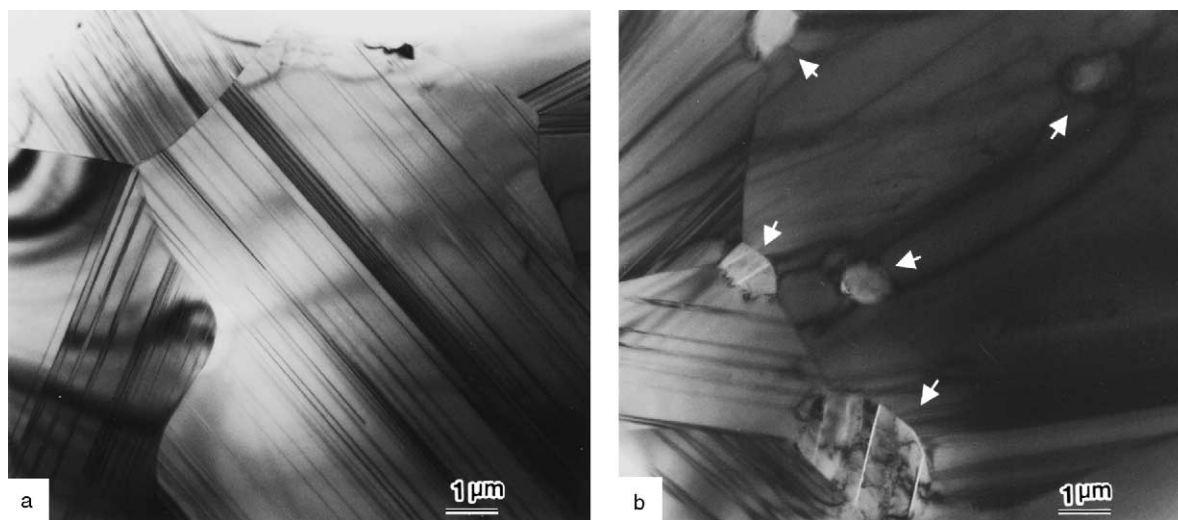

Fig. 2. Low-magnification TEM images of SiC ceramics with addition of BeO. SiC grains are densely packed in (a), and secondary phases are observed at triple-grain junction and in the grain in (b).

Table 1
Chemical compositions of impurities in SiC ceramics (mass percent)

Al	B	Be	Fe	O	N	Ti	V
0.030	<0.001	1.00	0.15	1.65	0.01	0.009	0.006

the impurities in the SiC ceramics. From the mass ratio of Be/O, oxygen was assumed to form mainly as a BeO phase. To clarify the distribution of impurity phases in SiC ceramics, characterization of the microstructure was performed by carefully using an electron diffraction method and EDS analysis in TEM observation.

Fig. 3 shows the typical form of the secondary phases in the ceramics. The inset is the selected area electron diffraction (SAD) pattern obtained from the crystalline phase at the triple-grain junction in Fig. 3(a). The figure shows that the reciprocal pattern projected the [1 0 0] zone axis of the BeO crystal, which has a hexagonal cell ($a = 0.270$, $c = 0.438$ nm). The BeO crystalline phase did not wet the SiC grains. Cracks were observed in the BeO crystalline phase, and an amorphous material was present in the cracks and around the BeO crystal. In addition, a contrast due to strain was observed between the BeO crystalline phase and the SiC grains. The cracks in the BeO grain were caused by the difference in the thermal expansion from that of the SiC matrix (BeO: 9.0×10^{-5} mm K^{-1}, SiC: 5.12×10^{-5} mm K^{-1}).[7] The amorphous material was composed of O and Al in addition to Si and C, as seen in Fig. 3(b). The Be atom was expected to be involved in the amorphous material, although this atom is not detected by the EDS detector. In Fig. 3(c), the oxygen atom was also detected from the two-grain boundary, which is indicated by arrows in Fig. 3(a). The boundary was approximately oriented in parallel to an electron beam.

The result of the EDS analysis indicated that the amorphous material also existed in the two-grain boundary. This was verified by a high-resolution TEM (HRTEM) observation.

Fig. 4 shows (a) the TEM image of a two-grain junction in the SiC ceramic and (b) an enlarged image of the region enclosed by the rectangle in (a). The boundary was not a straight line. When the grain boundary was oriented carefully in an edge-on condition, the HRTEM image revealed that an intergranular film of amorphous material with a width of about 0.6 nm was clearly present in the two-grain junction of the SiC ceramics.

There was on occasion a secondary phase at the triple-grain junction that possessed a different character and shape judging from the BeO crystalline phase in Fig. 5(a). The inset is a SAD pattern obtained from the secondary phase. Fig. 5(b) shows the EDS spectrum of the secondary phase. From the electron diffraction method and EDS analysis, it was determined to be Be_2SiO_4 with a trigonal cell (from ICSD data).

Fig. 6 shows (a) a low-magnification TEM image at a triple-grain junction, (b) the EDS spectrum obtained from the secondary phase indicated by the arrow in (a), and (c) and (d) enlarged TEM images of the region enclosed by the rectangle in (a). Inset in (a) is a SAD pattern of the SiC crystal. The secondary phase was composed of O, Fe, Si, Ti, and Ni, and these elements, except for Si, were impurities present in the SiC ceramics (Table 1) that were derived from the α-SiC source powder.[3] The impurity-crystalline phase seemed to be crystallized along the SiC grain surfaces; therefore, such precipitates should be crystallized from the liquid phase during the cooling process, as seen in AlN ceramics.[8,9] In Fig. 6(a) and (c), the orientation of the SiC crystal was set along the [1 0 0] axis, and the SiC grain seemed to contact
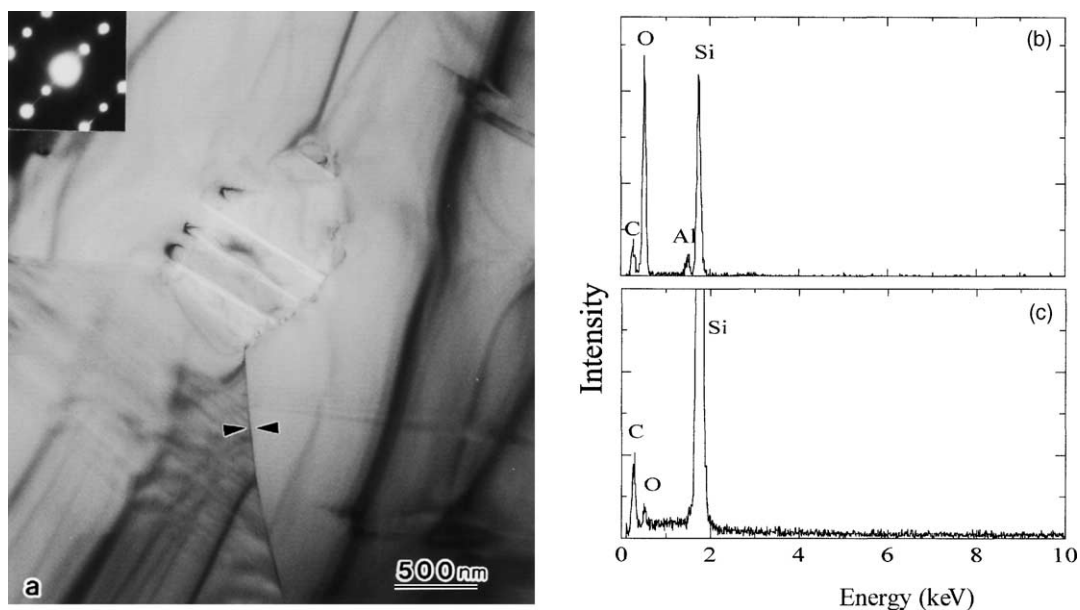

Fig. 3. (a) TEM image of secondary phase composed of BeO at the triple-grain junction in SiC ceramics, (b) EDS spectrum obtained from amorphous material in cracks in the secondary phase, and (c) EDS spectrum obtained from two-grain junction between two arrows.
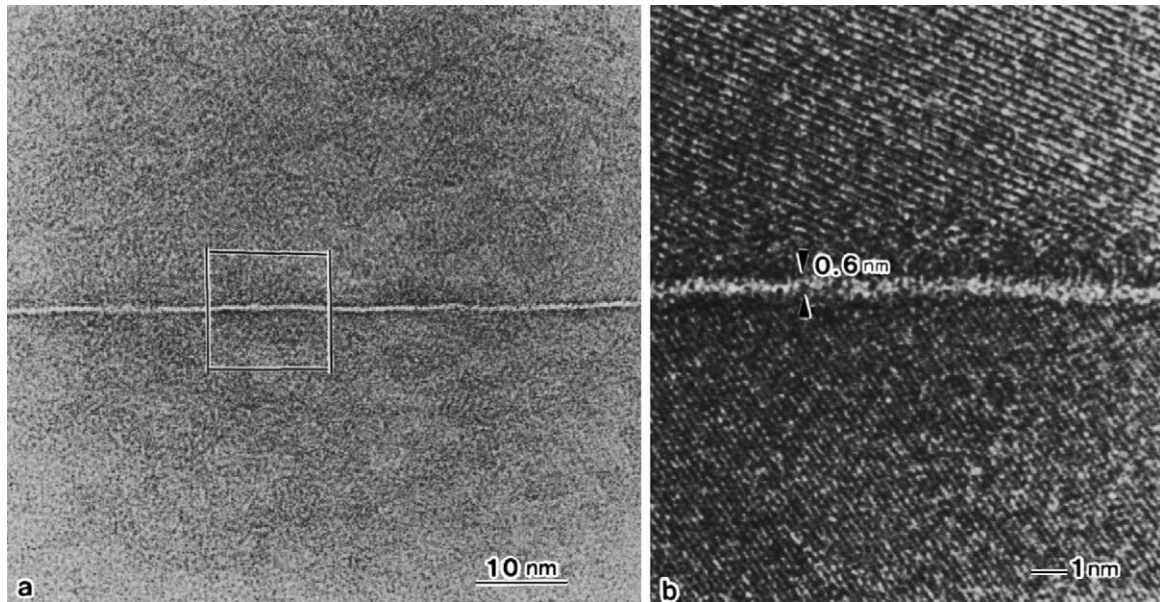
Fig. 4. (a) Low-magnification TEM image of two-grain junction of SiC ceramics and (b) high-resolution TEM image enclosed by the rectangle in (a). Intergranular film with a width of about 0.6 nm clearly existed in the two-grain junction.
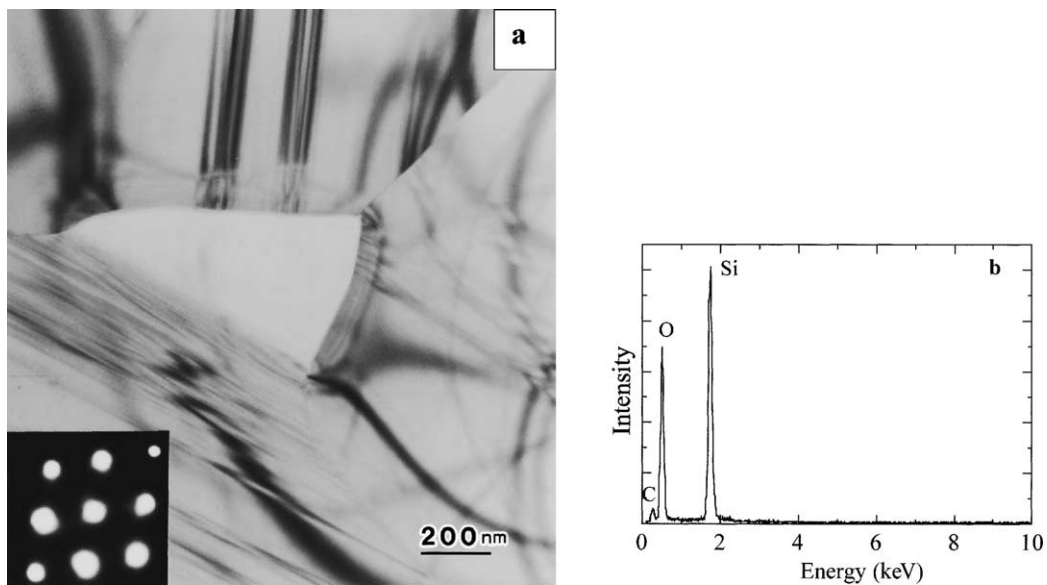

Fig. 5. (a) TEM image at triple-grain junction and SAD pattern of secondary phase composed of Be_2SiO_4 and (b) EDS spectrum obtained from the secondary phase. Be cannot be detected by the EDS detector.

directly with the impurity phase. However, when the plane of the boundary between the SiC grain and the secondary phase was set carefully parallel to the electron beam, which is the edge-on condition, the amorphous intergranular film was clearly observed at the boundary with a thickness of 1.3 nm, as shown in Fig. 6(d). This amorphous film was observed around the SiC grain and the precipitate. The periods of the lattice image of SiC perpendicular to the c-direction corresponded to those of the 6H- (1.5 nm) and 4H- (1.0 nm) SiC structures in Fig. 6(c). Other types of periodicity were also observed, and they were stacking disorders along the c-axis in SiC, as shown in streaks of SAD pattern along the c^*-direction.

4. Discussion

The microstructural evidence is summarized as a schematic illustration in Fig. 7. At the triple-grain junctions, BeO crystalline phases and the other types of secondary phases existed in the obtained SiC ceramics. The BeO crystalline phase was a hard crystal before the amorphous material became hard, as shown in Fig. 3. This is because the amorphous material entered the crack, caused by the difference in thermal expansion between BeO and SiC during the cooling process. Al was detected in the composition of the amorphous material, indicating that the impurity of the SiC grain was eliminated as in a zone-melting mechanism. The
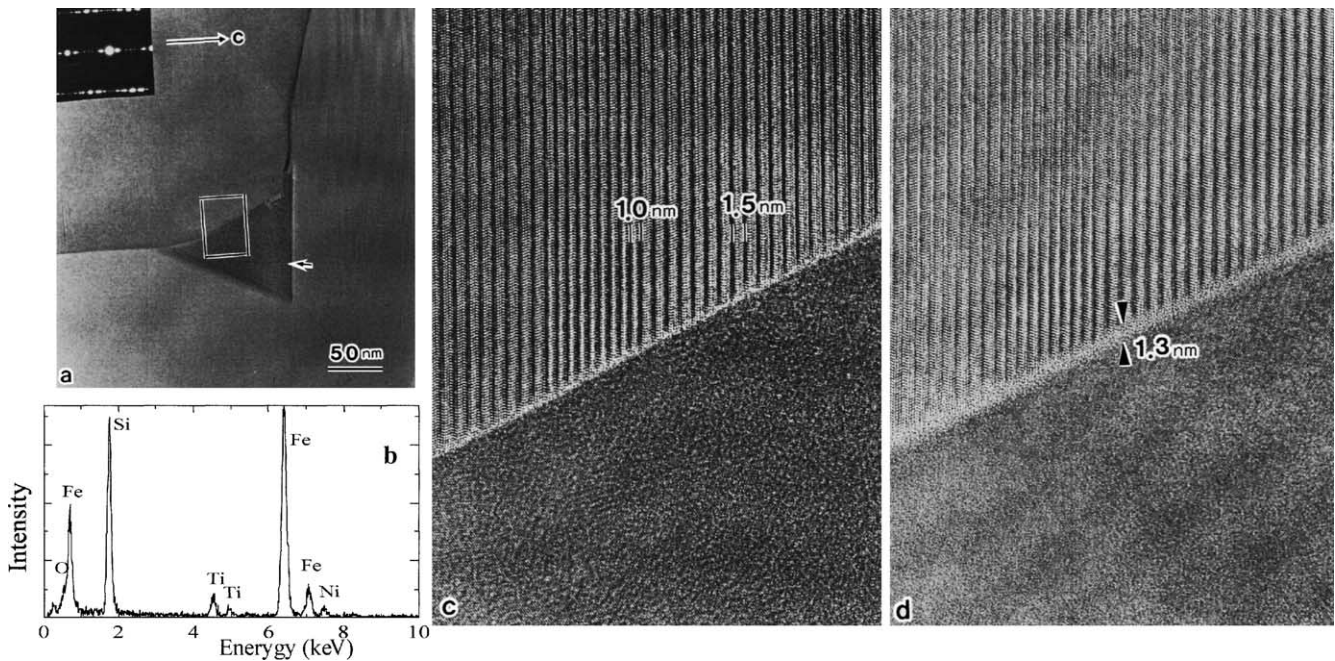
Fig. 6. (a) Low-magnification TEM image at triple-grain junction and SAD pattern of SiC grain along the [1 0 0] zone axis. (b) EDS spectrum obtained from the secondary phase indicated by the arrow in (a). (c and d) High-resolution TEM images enclosed by the rectangle in (a). SiC grain is oriented [1 0 0] zone axis in (c), and plane of the grain boundary between SiC and secondary phase is set to edge-on condition in (d).

other type of secondary phases (Figs. 5 and 6) were also precipitated from the liquid phase between the SiC grains. The existence of the Be_2SiO_4 crystalline phase indicated that a part of the SiC particles and the BeO additive dissolved at high-temperature with a composition in the ternary $BeO–SiO_2–SiC$ system. Impurity atoms, Fe, Ti, Al and Ni, were also trapped on the triple-grain junction during the liquid-sintering process, and, as a result, defects decreased in the SiC grain. Almost all of the SiC grains were separated from each other by an amorphous intergranular film of less than 1.0 nm width between them. This film contained O and perhaps Be in addition to Si and C. The chemical composition of the amorphous material was assumed to lie in the system, $BeO–SiO_2–SiC$. When the thickness of the
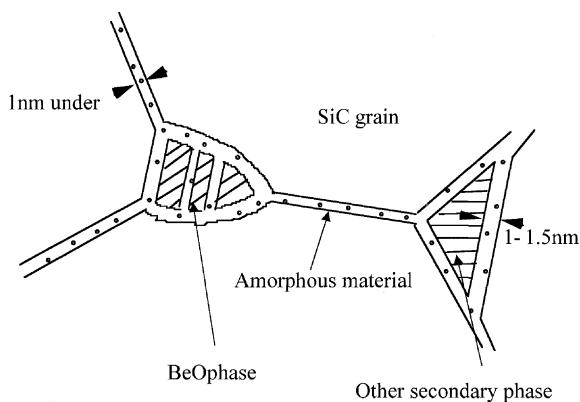

Fig. 7. Microstructural model of SiC added with BeO. Almost all of SiC grains were separated from each other by amorphous intergranular film.

grain boundaries is less than 1.0 nm, the observation of such an intergranular film is not easy by conventional TEM, and thus its characterization should be performed very carefully. Kaneko et al.[10] verified the presence of amorphous material in the boundary of β-SiC doped with B or C using HRTEM, STEM-HAADF and ELNES. However, some authors have stated that no intergranular film is found between two-grain junctions, even in SiC ceramics sintered with additives.[11,12] In the present case, an intergranular phase with thickness of less than 1 nm was found in many of the two-grain boundaries. The amorphous film's thickness around secondary phases was larger than that of the two-grain boundary. The equilibrium film thickness may be affected by the atomistic structure of the grain boundary glass, as seen in Si_3N_4.[13]

This work presents a detailed microstructure of the grains and grain boundaries. It is interesting to discuss the relationship between the thermal conductivity and the microstructure of the SiC ceramic. In Fig. 1, we showed the difference in thermal conductivity between the polycrystalline SiC ceramic with BeO addition and the single crystal (R66) at 5–1300 K. The difference was due to the microstructural defects and the presence of intergranular film between the SiC grains in the polycrystalline SiC ceramics. Those microstructures affect the thermal conductivity depending on the temperature. In this TEM study, we found cracks in the BeO crystalline phase and strain around the BeO particles, which were caused by the thermal expansion mismatch between SiC and BeO, as shown in Fig. 3. The streaks due to stacking disorder were also observed in the SiC lattice. Sakai and Aikawa reported[14] that the thermal conductivity

of SiC ceramics decreases appreciably with an increasing quantity of 4H SiC. The type of stacking disorder due to the SiC polytype is different from the case of the AlN polytype which arises from oxygen-related defects.[15] The existence of cracks and stacking defects is considered to be one of the causes of the reduced thermal conductivity. Jitendra et al. showed that the thermal conductivity is limited by a number of distinct phonon scattering mechanisms: intrinsic scattering, point-defect scattering, extended-defect scattering, dislocation scattering, and clean grain-boundary scattering.[16] Therefore, increases in thermal conductivity of SiC can be achieved by decreasing such defects because the value of $270\,\mathrm{W\,m^{-1}\,K^{-1}}$ is still half the intrinsic conductivity of SiC.

5. Conclusions

TEM observation revealed microstructural information for understanding the thermal conductivity of SiC ceramic with a value of $270\,\mathrm{W\,m^{-1}\,K^{-1}}$ at room temperature. Our findings in the present work include:

(1) In the SiC grain, streak-images due to stacking disorders were frequently observed, and the majority of structures were 6H- and 4H-types of SiC.
(2) Secondary phases were mainly composed of BeO introduced as an additive, and these crystalline phases were observed at the triple-grain junctions and even in the grains of SiC.
(3) Impurities, Fe, Ni, Al, Ti, and O were also precipitated at the triple-grain junctions during the liquid-phase sintering process, and, as a result, the defects in the SiC lattice decreased.
(4) HRTEM images revealed that a thin intergranular film with a thickness of less than 1 nm existed on the surfaces of almost all of the grains as an amorphous phase.

Acknowledgements

References

1. Goela, J. S., Brese, N. E., Pickering, M. A. and Graebner, J. E., Chemical-vapor-deposited materials for high thermal conductivity applications. *MRS Bull.* 2001, **26**, 458–463.
2. Watari, K., High thermal conductivity non-oxide ceramics. *J. Ceram. Soc. Jpn.* 2001, **109**, S7–S16.
3. Takeda, Y., Nakamura, K., Maeda, K. and Ura, M., Effects of elemental additives on densification, microstructure, strength, and thermal conductivity of silicon carbide ceramics. *Adv. Ceram. Mater.* 1986, **1**, 162–165.
4. Takeda, Y., Ogihara, S. and Maeda, K., Effect of additives on thermal conductivity and electrical resistivity of SiC ceramics. *J. Ceram. Soc. Jpn.* 1988, **95**, 860–863.
5. Slack, G. A., Thermal conductivity of pure and impure silicon, silicon carbide and diamond. *J. Appl. Phys.* 1964, **35**, 3460–3466.
6. Watari, K., Nakano, H., Sato, K., Urabe, K., Ishizaki, K., Cao, S. *et al.*, Effect of grain boundaries on thermal conductivity of SiC ceramic at 5–1300 K. *J. Am. Ceram. Soc.* 2003, **86**(10), 1812–1814.
7. Committee of Fine Ceramic Ziten, *Fine Ceramics Ziten*. Gihodo Press, 1987 [in japanese].
8. Nakano, H., Watari, K. and Urabe, K., Grain boundary phase in AlN ceramics fired under reducing N_2 atmosphere with carbon. *J. Eur. Ceram. Soc.* 2003, **23/10**, 1761–1768.
9. Nakano, H., Watari, K., Hayashi, H. and Urabe, K., Microstructural characterization of high-thermal-conductivity alminum nitride ceramic. *J. Am. Ceram. Soc.* 2002, **85**(12), 3093–3095.
10. Kaneko, K., Kawasaki, M., Nagano, T., Tamari, N. and Tsurekawa, S., Determination of the chemical width of grain bounadry of moron- and carbon-doped hot-pressed β-SiC by HAADF imaging and ELNES line-profile. *Acta Mater.* 2000, **48**, 903–910.
11. Takeda, Y., Nakamura, H., Maeda, K. and Matsushita, Y., Effects of additives on thermal conductivity and electrical resistivity of SiC ceramics. *Yogyo-kyokai-shi* 1987, **95**(9), 860–863 [in Japanese].
12. Nakamura, H., Maeda, K., Takeda, Y. and Ura, M., New SiC ceramics with high thermal conductivity and high electrical resistivity. *Oyo Butsuri* 1984, **53**(4), 311–314.
13. Kleebe, H.-J., Structure and chemistry of interfaces in Si_3N_4 ceramics, studied by transmission electron microscopy. *J. Ceram. Soc. Jpn.* 1997, **105**(6), 453–475.
14. Sakai, T. and Aikawa, T., Phase transformation and thermal conductivity of hot-pressed silicon carbide containing alumina and carbon. *J. Am. Ceram. Soc.* 1988, **71**, C7–C9.
15. Hagege, S., Tanaka, S. and Ishida, Y., Structural analysis of planar defects in wurtzite type aluminum nitride. *J. Jpn. Inst. Metals* 1988, **52**(12), 1192–1198 [in Japanese].
16. Jitendra, S. G., Nathaniel E. B., Michael, A. P. and John, E. G., Chemical-vapor-deposited materials for high thermal conductivity applications. *MRS Bull.* June (2001) 458–463.